Nano Research 2015, 8(12): 3815–3822
DOI 10.1007/s12274-015-0881-0
Research Article

ISSN 1998-0124
CN 11-5974/O4

Facile synthesis of Fe/Ni bimetallic oxide solid-solution nanoparticles with superior electrocatalytic activity for oxygen evolution reaction

Lingxiao Wang, Jing Geng, Wenhai Wang, Chao Yuan, Long Kuai, and Baoyou Geng (✉)

College of Chemistry and Materials Science, The Key Laboratory of Functional Molecular Solids, Ministry of Education, Anhui Laboratory of Molecular-Based Materials, Center for Nano Science and Technology, Anhui Normal University, No.1 Beijing East Road, Wuhu 241000, China

Received: 1 August 2015
Revised: 10 August 2015
Accepted: 16 August 2015

KEYWORDS

Fe-Ni-O_x,
solid solution,
electrocatalysis,
oxygen evolution reaction

ABSTRACT

The sluggish oxygen evolution reaction (OER) is an important half-reaction of the electrochemical water-splitting reaction. Amorphous Fe/Ni composite oxides have high activity. In this work, we modified the aerosol spray-assisted approach and obtained amorphous Fe-Ni-O_x solid-solution nanoparticles (Fe-Ni-O_x-NPs) approximately 20 nm in size by choosing iron/nickel acetylacetonates as raw materials instead of inorganic salts. The small-sized Fe-Ni-O_x-NPs were characterized by scanning electron microscopy (SEM), transmission electron microscopy (TEM), X-ray diffraction (XRD) analysis, energy-dispersive X-ray spectroscopy (EDX), and X-ray photoelectron spectroscopy (XPS). Furthermore, an investigation of electrochemical OER performance suggests that the small-sized Fe-Ni-O_x-NPs have higher activity than the large-sized Fe-Ni-O_x-MPs. A small overpotential of 0.315 V was demanded to obtain a working current density of 50 mA/cm^2, and the Tafel slope was as low as 38 mV/dec.

1 Introduction

The oxygen evolution reaction (OER) is an important half-reaction of the water-splitting reaction [1–4]. The other simultaneous half-reaction (HER) produces hydrogen [5–8], a clean energy that can slightly ease the tension caused by fossil fuels. Because of the slow kinetics, a desirable electrocatalyst is eagerly discovered to increase the rate of the OER. At present, noble metals (e.g., IrO_x) are used in the water-splitting reaction because of their excellent HER or OER activity [9, 10]; however, these precious metals have a very rare distribution of elements in the crust. Thus, much effort has been expended searching for earth-abundant metals capable of substituting for noble metals. Among these materials, nickel compounds have attracted much attention owing to its high OER activity [11–13]. Furthermore, the activity can be

Address correspondence to bygeng@mail.ahnu.edu.cn

notably enhanced when doping Fe in the Ni structure [14, 15]. One of the reasons for this enhancement is that the conductivity of a Ni–Fe catalyst is dramatically improved as compared to that of a pure Ni catalyst [14]. Another reason is that Fe exerts a partial-charge-transfer activation effect on Ni, making it more difficult to oxidize Ni^{2+}. This leads to the formation of $Ni^{3+/4+}$, which has more oxidizing power, thus increasing the OER kinetics [15–17]. Many works have also revealed that a composite nickel oxide mixed with 10%–50% iron shows favorable properties in terms of decreasing the Tafel slope and the overpotential, resulting in excellent catalytic stability [14, 18–21].

Amorphous metal oxides have been recently found to possess much higher activity for OER than crystallized ones, especially precious metal-free Fe/Ni-based multicomponent oxides [9, 10, 20]. Up to now, electrochemical deposition [14, 22–24], photochemical metal organic decomposition [10, 20, 25], the reactive magnetron co-sputtering technique [26], and the solvothermal method [27] have been developed to access amorphous oxides or films for electrochemical OER. Recently, we used an aerosol-spray-assisted approach (ASAA) to realize the fast pyrolysis of salts and obtain amorphous Fe-Ni-O_x microspheres with good control of the proportions of Fe/Ni, scalable production ability, and high activity for OER [28]. However, there is a problem in that the size of the catalyst powder is as large as hundreds of nanometers, which limits the utilization efficiency of the catalyst (mass activity). Thus, it is desirable to modify the ASAA method to obtain nanosized catalysts.

In this work, we obtained amorphous Fe-Ni-O_x solid-solution nanoparticles (Fe-Ni-O_x-NPs) approximately 20 nm in size by choosing iron/nickel acetylacetonates as raw materials instead of inorganic salts. The iron/nickel acetylacetonates are an order of magnitude smaller than the raw materials used in our previous work, which were hundreds of nanometers in size (Fe-Ni-O_x-MPs). As expected, the Fe-Ni-O_x NPs exhibited higher activity than the Fe-Ni-O_x-MPs. We just need a small overpotential of 0.315 V to acquire a high OER current density of 50 mA/cm^2, and a low Tafel slope of 38 mV/dec were observed. Therefore, the obtained Fe-Ni-O_x solid-solution NPs can be potential electrode materials for electrochemical water splitting.

2 Experimental

2.1 Chemicals

Nickel acetylacetonate [$Ni(acac)_2$], iron acetylacetonate [$Fe(acac)_3$], and potassium hydroxide (KOH) were bought from Aladdin (China). The nitrates $Fe(NO_3)_3\cdot 9H_2O$ and $Ni(NO_3)_2\cdot 6H_2O$ and N,N-dimethyl formamide (DMF) were obtained from Shanghai Reagent Co. Ltd. Conductive carbon black (Vulcan® XC-72) was purchased from Carbot (Shanghai). All the chemicals were of analytical grade and were used as received without any further purification. The Nafion® (5 wt.%) solution was obtained from Dupont Co. Ltd. The resistance of the water used in this work was more than 18 MΩ.

2.2 Materials synthesis

In this experiment, a Fe-Ni-O_x solid solution was synthesized by the fellow process: 0.1712 g (0.667 mmol) of $Ni(acac)_2$ and 0.1177 g (0.332 mmol) of $Fe(acac)_3$ were added to 10 mL of absolute ethanol. 6 mL of DMF was then added to obtain a homogeneous reddish-brown solution. The above solution was transferred to a medical-use ultrasonic humidifier (1.7 MHz, 35 W) for aerosol generation. The liquid spray was drawn into a tube furnace that was preheated to 400 ˚C by a vacuum pump. The products denoted as Fe-Ni-O_x-NPs were collected through filtration. The mole ratio of Fe/Ni was 1:2.

For comparison, a kelly solution was obtained by ultrasonically dissolving 0.1938 g (0.667 mmol) of $Ni(NO_3)_2\cdot 6H_2O$ and 0.1346 g (0.332 mmol) of $Fe(NO_3)_3\cdot 9H_2O$ in 10 mL water. The rest of the steps are the same as those described above. The products were marked as Fe-Ni-O_x-MPs. The molar ratio of Fe/Ni was 1:2.

2.3 Characterization

The morphology of the as-prepared materials were characterized with scanning electron microscopy (SEM, Hitachi S-4800, Japan), with a 5 kV accelerating voltage, and transmission electron microscopy (TEM, Tecnai G2 20 S-TWIN), with a 200 kV accelerating voltage. The elemental analysis was conducted by SEM (Hitachi S-4800, Japan) equipped with energy-dispersive X-ray spectroscopy (EDX), with a 15 kV accelerating voltage. The phase identification was executed by X-ray

diffraction (XRD, Cu Kα radiation, λ = 0.154,056 nm) analysis. The surface composition was determined using X-ray photoelectron spectroscopy (XPS, ESCALAB 250, Mg Kα X-ray source) at 15 kV.

2.4 Electrochemical measurements

2 mg of the active catalyst powder was dispersed in a mixed water and N,N-dimethyl formamide (2:1, *V*/*V*) solution (0.4 mL), and then 5 μL of Nafion® solution (5 wt.%) and 1 mg of carbon black (Vulcan® XC-72) were added. To prepare a homogeneous ink, the suspension was treated under continuous ultrasonication for approximately 5 min. Subsequently, 4 μL of the catalyst ink was dripped onto a clean glassy carbon electrode with a diameter of 3 mm (active materials loading 0.28 mg/cm^2) and then dried at room temperature. We noted that, prior to catalyst loading, the glassy carbon electrode was polished with alumina (0.05 μm in diameter) slurries under sonication in water after each polish.

The electrochemical measurements were performed using an electrochemical workstation (CHI660C, Shanghai, China) in a three-electrode system in a fresh 1 M KOH solution at room temperature. The counter electrode was a coiled platinum wire, and a Hg/HgO electrode (1 M KOH) was used as a reference electrode. All potentials reported in the measurements are measured against this Hg/HgO reference with a potential of 0.131 V versus the standard hydrogen electrode (SHE). The cyclic voltammetry (CV) and linear sweep voltammetry (LSV) curves were all obtained at a sweep rate of 10 mV/s and a quiet time of 5 s. The electrochemical AC impedance spectra were performed at 0.6 V versus Hg/HgO with frequency ranging from 100 kHz to 0.1 Hz with a amplitude of 2 mV and a quiet time of 5 s. In addition, the electrolyte solution was bubbled with O_2 (99.4% purity) to keep the equilibrium potential of O_2/OH^- at 1.23 V (versus RHE).

All the potentials were 100% IR-corrected. The resistances (*R*) were obtained from the electrochemical AC impedance spectra.

3 Results and discussion

3.1 Morphology and structural characterization

The process for the small-sized Fe-Ni-O_x NP preparation is similar to the previous work [28–30]. The ratio of 1:2 between Fe and Ni is chosen to get a high activity based on the precious work on the Fe/Ni composition-dependent activity [14, 25, 28]. The SEM image in Fig. 1(a) shows that the products made with acetylacetonates consist of small-sized Fe-Ni-O_x NPs approximately 20 nm in size. The TEM image in Fig. 1(b) shows that the small-sized Fe-Ni-O_x NPs have a rough surface. For comparison, microsized Fe-Ni-O_x MPs were

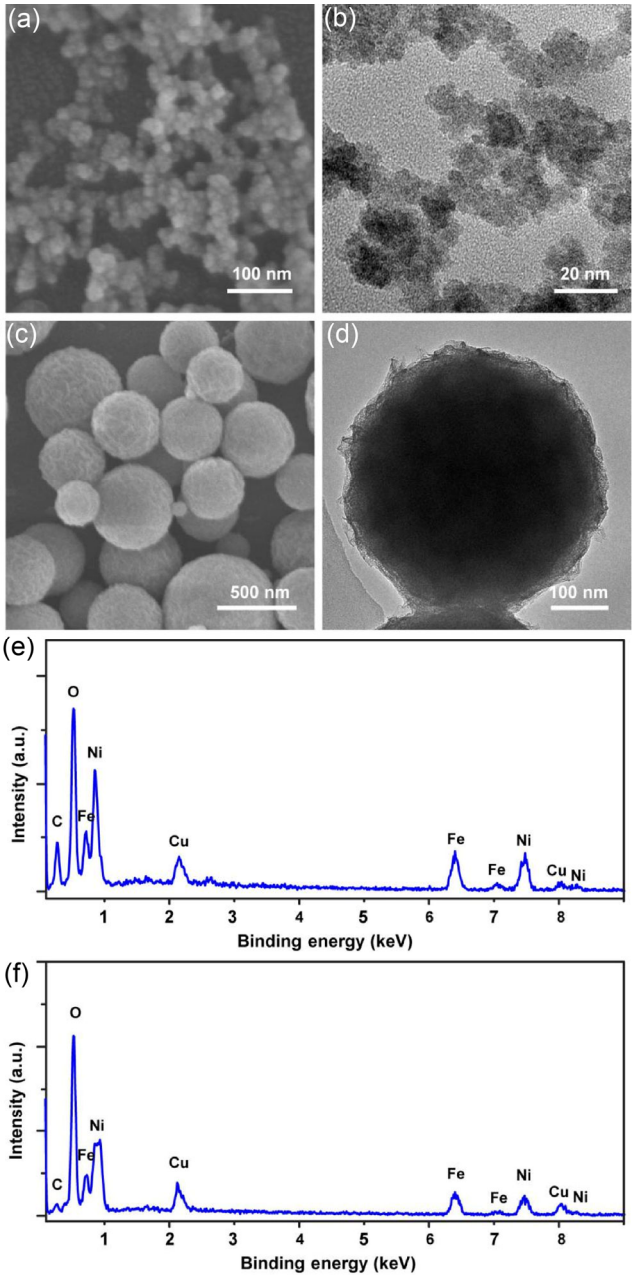

Figure 1 (a) and (c) SEM and (b) and (d) TEM images, (e) and (f) EDX spectra of Fe-Ni-O_x NPs ((a), (b), and (e)) and Fe-Ni-O_x MPs ((c), (d), and (f)).

also prepared as per a previously reported method, in which inorganic salts were used as raw materials [28]. As shown in Figs. 1(c) and 1(d), the Fe-Ni-O_x-MPs made with metal nitrates are microspheres whose sizes range from 0.23 to 0.45 μm, which is an order of magnitude larger than the Fe-Ni-O_x NPs. Subsequently, EDX analysis (Figs. 1(e) and 1(f)) confirmed the composition of Fe-Ni-O_x NPs and Fe-Ni-O_x MPs. The O, Ni, and Fe elements were from the Fe-Ni-O_x catalysts, and the Cu peaks are ascribed to the Cu substrate used for EDX measurements. No other impurities were found in the products.

The reason for the nanosized Fe-Ni-O_x solid-solution formation may have been the suitable size of the raw materials. Careful observation of the Fe-Ni-O_x MPs (Fig. S1 in the Electronic Supplementary Material (ESM) and Fig. 1(d)) reveals that the microspheres are self-assembled by ultrathin nanosheets (surface part) and nanoparticles (inner part) with sizes of approximately 5 nm. Because there was no capping agent in the preparation system, the high surface energy induced these primary nanoparticles to aggregate together. When the size of the Fe-Ni-O_x NPs was approximately 20 nm, the surface energy was insufficient to induce self-assembly into larger-sized microspheres. As a result, dispersive nanoparticles formed, although they seemed to adhere to each other to a certain extent. Successively, we discuss why the nanosheets are formed in the Fe-Ni-O_x-MPs. The formation of Fe-Ni-O_x products consists of two steps: 1) evaporation of the solvent and 2) pyrolysis of the precursors. In the case of inorganic salts as precursors, a few metal hydroides may have formed through metal ion hydrolysis during solvent evaporation. It is well known that metal hydroxides easily grow into nanosheets owing to their layered structure [15, 21, 31, 32]. Because solvent evaporation is much faster than the hydrolysis of metal ions, the proportion of nanosheets is much lower than that of nanoparticles in the microspheres formed by the subsequent pyrolysis of nitrates. However, the hydrolysis of metal ions with acetylacetonates is negligible in an organic solvent. As a result, no metal hydroide nanosheets were formed.

To confirm the phase and crystallization degree of the products, XRD analysis of Fe-Ni-O_x solid-solution NPs and Fe-Ni-O_x MPs were carried out. As shown in Fig. 2, the broad peak centered at approximately 22° was assigned to the amorphous glass substrate, and no obvious diffraction signal was observed for either the Fe-Ni-O_x NPs (red) or the Fe-Ni-O_x MPs (black), indicating that both of them had an amorphous structure. The triple peaks at 37.3°, 43.3°, and 62.9° of crystalline NiO from the standard card (PDF No. 1-1239) are labeled in the XRD pattern (blue). However, these peaks were barely observed in the two products. We only find the ultra-weak and highly broad bulge, which may stem from a few short- or medium-ordered oxide clusters. In addition, the size of Fe-Ni-O_x NPs was approximately 20 nm based on the SEM and TEM observation. The NPs would show strong and sharp XRD peaks if they were crystalline. However, the results of the XRD patterns show that this is not the case.

XPS analysis (Fig. S2 in the ESM and Fig. 3) was performed to study the surface chemical environment of the Fe-Ni-O_x NPs [33]. According to the fitted $Ni2p_{3/2}$ spectra (Fig. 3(a)), we found that the surface Ni consisted of Ni–O and Ni–OH bonds, indicating that the surface was adsorbed by hydroxyl. As for surface Fe (Fig. 3(b)), the Fe–O bond is dominant. Consistent with the chemical state of the surface metals, the surface O atoms comprised three types of oxygen: lattice O, –OH, and H_2O, with corresponding proportions of 38.6%, 57.3%, and 4.1%, respectively, as shown in Fig. 3. Smith et al. showed that there was a negative correlation between the relative concentrations of hydroxyl surface groups to the lattice oxygen and the Tafel slope of OER and that approximately

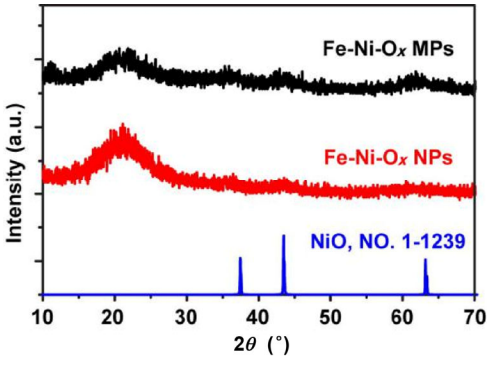

Figure 2 XRD patterns of Fe-Ni-O_x NPs (red), Fe-Ni-O_x MPs (black), and the standard card of NiO with PDF number of 1-1239.

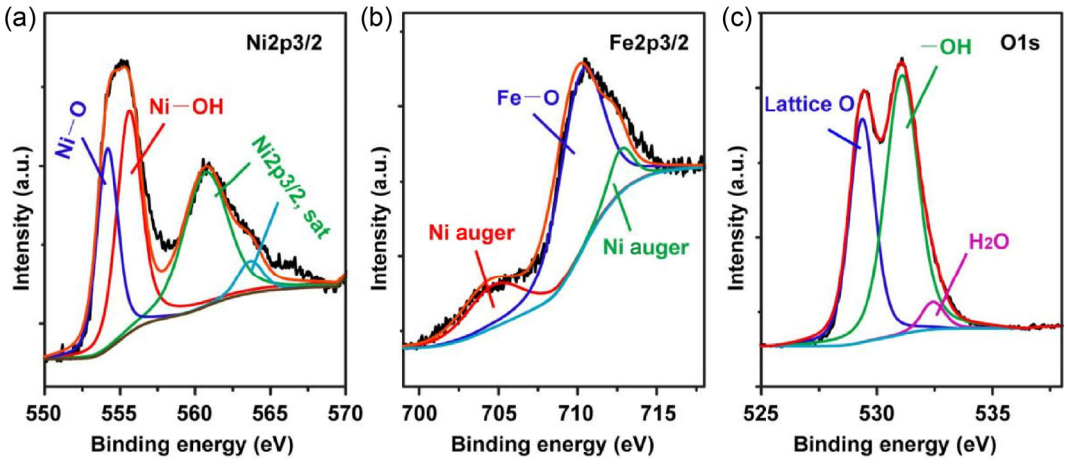

Figure 3 XPS spectra of (a) Ni2$p_{3/2}$, (b) Fe2$p_{3/2}$, and (c) O1s of Fe-Ni-O_x NPs.

70% –OH possession would decrease the Tafel slope to as low as 34 mV/dec [20]. Therefore, the lower –OH content is beneficial for obtaining a low Tafel slope for OER, which is in good agreement with the corresponding Tafel slope of 38 mV/dec in the subsequent electrochemical study.

3.2 Electrochemical oxygen evolution investigation

To evaluate the activity of the obtained small-sized amorphous Fe-Ni-O_x NPs, we prepared an Fe-Ni-O_x NP-modified glassy carbon electrode for oxygen evolution in alkaline media (1 M KOH). For comparison, large-sized Fe-Ni-O_x NPs, Vulcan® XC-72 carbon black, and a bare glassy carbon (GC) electrode were also studied. As shown in Fig. 4(a), the CV curves for both the Fe-Ni-O_x NPs and the Fe-Ni-O_x MPs exhibit a redox couple whose peaks are the result of the transformation between surface Ni^{II} and Ni^{III} in alkaline media. The reaction equation is $Ni(OH)_2 + OH^- \rightarrow NiOOH + H_2O + e^-$ [15]. Moreover, the oxidation currents after Ni oxidation are the result of the evolution of oxygen, $4OH^- \rightarrow O_2 + 2H_2O + 4e^-$. According to previous reports [14, 15], we know that if the Fe content of a nickel iron oxide increases, the Ni^{II}/Ni^{III} redox couple will move to higher potentials, the peak area will decrease, and the oxidation wave will be less visible because Ni^{II} is more difficult to oxidize after Fe doping. From the CV curves, we see that the Ni^{II}/Ni^{III} redox

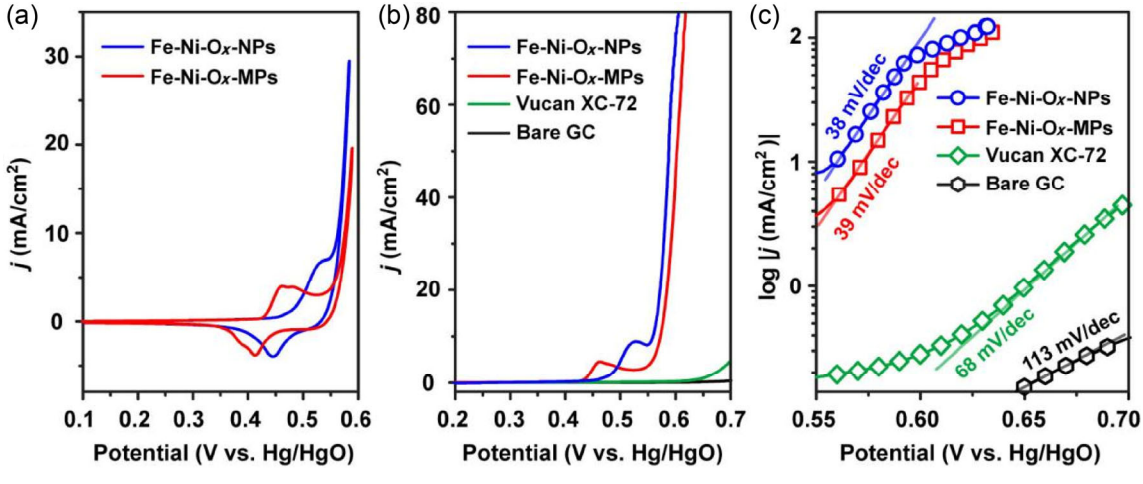

Figure 4 (a) CV curves, (b) LSV curves, and (c) Tafel plots of Fe-Ni-O_x NPs (blue), Fe-Ni-O_x MPs (red), Vulcan® XC-72 carbon (green), and a bare glassy carbon electrode substrate (black) in 1 M KOH at a scanning rate of 10 mV/s.

couple peaks of the Fe-Ni-O_x NPs are more positive, which means that the Fe was more successfully doped into the NiO matrix. In addition, the oxidation peak for the Fe-Ni-O_x NPs (blue) is more positive than that for the Fe-Ni-O_x MPs (red) and the peak area is larger than that of the Fe-Ni-O_x MPs, which suggests that the Fe-Ni-O_x NPs catalysts have more active sites than the Fe-Ni-O_x MPs due to their much smaller size.

Figure 4(b) displays the LSV polarization curves of OER catalyzed by the above-mentioned electrodes. We can see that the contribution of carbon black (green) and the bare GC electrode (black) can be neglected in the discussion of the amorphous Fe-Ni-O_x catalysts. More importantly, as compared to the Fe-Ni-O_x MPs (red), an apparently lower potential is required for Fe-Ni-O_x NPs (blue) to obtain the same OER current density (j). Typically at a current density of 10 mA/cm^2, the Fe-Ni-O_x NP catalyst exhibits an overpotential that is 13 mV lower (0.286 V) than that of the Fe-Ni-O_x MPs (0.299 V), which can be ascribed to the small size, resulting in a higher surface area and a shorter ion diffusion length. Furthermore, a small overpotential of 0.315 V can induce a high OER j of 50 mA/cm^2, whereas only approximately 23 mA/cm^2 can be obtained with the Fe-Ni-O_i MP-modified electrode at the same potential. Furthermore, as shown in Fig. 4(c), the Tafel slopes (based on the Tafel equation: $\eta = a + b \log j$, where η represents the overpotential and a and b are constants [34]) for the Fe-Ni-O_x NPs (blue) and Fe-Ni-O_x MPs (red) are as low as 38 and 39 mV/dec, respectively, which are consistent with previous reports [20, 25]. The low Tafel slopes suggest the low activation energy for electrochemical OER. In addition, the Tafel slopes of Vulcan® XC-72 carbon (green) black and the bare GC (black) electrode are as high as 68 and 113 mV/dec, respectively.

The electrochemical impedance spectra (EIS) were performed to study the charge transfer resistance (R_{ct}), with the testing potential of 0.6 V versus Hg/HgO, a frequency scan range from 100 kHz to 0.1 Hz, and an amplitude of 2 mV. It is known that a simple electrochemical interface is built up with the paralleling components of a double layer capacitor and Faradaic resistance [35]. In the Nyquist plots of EIS, the diameter of a semicircle stands for the R_{ct}. As displayed in Fig. 5, the electrocatalyst of the Fe-Ni-O_x NPs (blue) has the minimum diameter of the semicircle, which indicates the smallest R_{ct} value (~8 Ω) of the fours. Besides, the R_{ct} of the Fe-Ni-O_x MPs (red) (~19 Ω) is more than one-fold higher than that of the Fe-Ni-O_x NPs. Successively, much larger Faradaic resistance was obtained from the Vulcan® XC-72 carbon black (green) and the bare GC electrode (black). The above observations suggest that small-sized Fe-Ni-O_x NPs, possessing more active sites and a higher active surface area, have a faster rate of charge transfer owing to high kinetics for the OER.

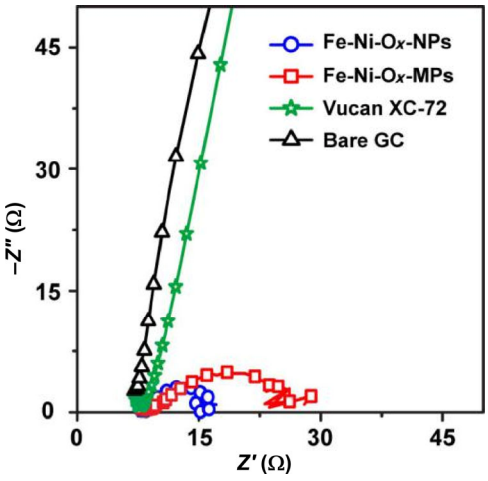

Figure 5 Nyquist plots of electrochemical impedance spectra of Fe-Ni-O_x NPs (blue), Fe-Ni-O_x MPs (red), Vulcan® XC-72 carbon (green), and bare glassy carbon electrode substrate (black) under OER conditions.

4 Conclusions

A small-sized amorphous Fe-Ni-O_x NPs approximately 20 nm in size possessing more active sites and higher active surface areas were prepared with an aerosol spray-assisted approach by using iron/nickel acetylacetonates as the raw materials instead of inorganic salts. The electrochemical measurements for the OER indicate that Fe-Ni-O_x NPs exhibited better performance than the large-sized Fe-Ni-O_x NPs obtained with nitrates as raw materials. A small overpotential of 0.315 V induced a current density of 50 mA/cm^2, resulting in a Tafel slope as low as 38 mV/dec. The outstanding performance of the Fe-Ni-O_x NPs originates from the small size and the amorphous property of the Fe/Ni bimetallic oxide. Moreover, Fe-Ni-O_x NPs could potentially be applied to electrocatalysis of OER

in water splitting and rechargeable metal–air batteries in the future.

Acknowledgements

This work was supported by the National Natural Science Foundation of China (Nos. 21271009 and 21471006), the Doctoral Fund of the Ministry of Education of China (No. 20123424110002), the National Undergraduate Training Programs for Innovation and Entrepreneurship (No. 201410370043), and the Programs for Science and Technology Development of Anhui Province (No. 1501021019).

Electronic Supplementary Material: Supplementary material (high-magnification TEM image of Fe-Ni-O_x MPs and XPS survey of Fe-Ni-O_x NPs) is available in the online version of this article at http://dx.doi.org/10.1007/s12274-015-0881-0.

References

[1] Man, I. C.; Su, H.-Y.; Calle-Vallejo, F.; Hansen, H. A.; Martínez, J. I.; Inoglu, N. G.; Kitchin, J.; Jaramillo, T. F.; Nørskov, J. K.; Rossmeisl, J. Universality in oxygen evolution electrocatalysis on oxide surfaces. *ChemCatChem* **2011**, *3*, 1159–1165.

[2] Ma, W.; Ma, R. Z.; Wang, C. X.; Liang, J. B.; Liu, X. H.; Zhou, K. C.; Sasaki, T. A superlattice of alternately stacked Ni-Fe hydroxide nanosheets and graphene for efficient splitting of water. *ACS Nano* **2015**, *9*, 1977–1984.

[3] Tüysüz, H.; Hwang, Y. J.; Khan, S. B.; Asin, A. M.; Yang, P. D. Mesoporous Co_3O_4 as an electrocatalyst for water oxidation. *Nano Res.* **2013**, *6*, 47–54.

[4] Geng, J.; Kuai, L.; Kan, E. J.; Wang, Q.; Geng, B. Y. Precious-metal-free Co-Fe-O/rGO synergetic electrocatalysts for oxygen evolution reaction by a facile hydrothermal route. *ChemSusChem* **2015**, *8*, 659–664.

[5] Chen, Z. B.; Cummins, D.; Reinecke, B. N.; Clark, E.; Sunkara, M. K.; Jaramillo, T. F. Core-shell MoO_3-MoS_2 nanowires for hydrogen evolution: A functional design for electrocatalytic materials. *Nano Lett.* **2011**, *11*, 4168–4175.

[6] Popczun, E. J.; Read, C. G.; Roske, C. W.; Lewis, N. S.; Schaak, R. E. Highly active electrocatalysis of the hydrogen evolution reaction by cobalt phosphide nanoparticles. *Angew. Chem., Int. Ed.* **2014**, *53*, 5427–5430.

[7] Gong, M.; Zhou, W.; Tsai, M.-C.; Zhou, J. G.; Guan, M. Y.; Lin, M.-C.; Zhang, B.; Hu, Y. F.; Wang, D.-Y.; Yang, J. et al. Nanoscale nickel oxide/nickel heterostructures for active hydrogen evolution electrocatalysis. *Nat. Commun.* **2014**, *5*, 4695.

[8] Tian, J. Q.; Liu, Q.; Asiri, A. M.; Sun, X. P. Self-supported nanoporous cobalt phosphide nanowire arrays: An efficient 3D hydrogen-evolving cathode over the wide range of pH 0–14. *J. Am. Chem. Soc.* **2014**, *136*, 7587−7590.

[9] Tsuji, E.; Imanishi, A.; Fukui, K.; Nakato, Y. Electrocatalytic activity of amorphous RuO_2 electrode for oxygen evolution in an aqueous solution. *Electrochim. Acta* **2011**, *56*, 2009–2016.

[10] Smith, R. D. L.; Sporinova, B.; Fagan, R. D.; Trudel, S.; Berlinguette, C. P. Facile photochemical preparation of amorphous iridium oxide films for water oxidation catalysis. *Chem. Mater.* **2014**, *26*, 1654−1659.

[11] Singh, A.; Chang, S. L. Y.; Hocking, R. K.; Bachcde, U.; Spiccia, L. Highly active nickel oxide water oxidation catalysts deposited from molecular complexes. *Energy Environ. Sci.* **2013**, *6*, 579–586.

[12] Gao, M. R.; Sheng, W. C.; Zhuang, Z. B.; Fang, Q. R.; Gu, S.; Jiang, J.; Yan, Y. S. Efficient water oxidation using nanostructured α-nickel-hydroxide as an electrocatalyst. *J. Am. Chem. Soc.* **2014**, *136*, 7077–7084.

[13] Nadesan, J. C. B.; Tseung, A. C. C. Oxygen evolution on nickel oxide electrodes. *J. Electrochem. Soc.* **1985**, *132*, 2957–2959.

[14] Corrigan, D. A. The catalysis of the oxygen evolution reaction by iron impurities in thin film nickel oxide electrodes. *J. Electrochem. Soc.* **1987**, *134*, 377–384.

[15] Trotochaud, L.; Young, S. L.; Ranney, J. K.; Boettcher, S. W. Nickel–iron oxyhydroxide oxygen-evolution electrocatalysts: The role of intentional and incidental iron incorporation. *J. Am. Chem. Soc.* **2014**, *136*, 6744–6753.

[16] Yeo, B. S.; Bell, A. T. *In situ* Raman study of nickel oxide and gold-supported nickel oxide catalysts for the electrochemical evolution of oxygen. *J. Phys. Chem. C* **2012**, *116*, 8394–8400.

[17] Corrigan, D. A.; Conell, R. S.; Fierro, C. A.; Scherson, D. A. *In-situ* Mössbauer study of redox processes in a composite hydroxide of iron and nickel. *J. Phys. Chem.* **1987**, *91*, 5009–5011.

[18] Louie, M. W.; Bell, A. T. An investigation of thin-film Ni–Fe oxide catalysts for the electrochemical evolution of oxygen. *J. Am. Chem. Soc.* **2013**, *135*, 12329–12337.

[19] Yu, X. W.; Zhang, M.; Yuan, W. J.; Shi, G. Q. A high-performance three-dimensional Ni–Fe layered double hydroxide/graphene electrode for water oxidation. *J. Mater. Chem. A* **2015**, *3*, 6921–6928.

[20] Smith, R. D. L.; Prévot, M. S.; Fagan, R. D.; Trudel, S.; Berlinguette, C. P. Water oxidation catalysis: Electrocatalytic response to metal stoichiometry in amorphous metal oxide films containing iron, cobalt, and nickel. *J. Am. Chem. Soc.* **2013**, *135*, 11580–11586.

[21] Gong, M.; Li, Y. G.; Wang, H. L.; Liang, Y. Y.; Wu, J. Z.; Zhou, J. G.; Wang, J.; Regier, T.; Wei, F.; Dai, H. J. An advanced Ni–Fe layered double hydroxide electrocatalyst for water oxidation. *J. Am. Chem. Soc.* **2013**, *135*, 8452–8455.

[22] Lu, X. Y.; Zhao, C. Electrodeposition of hierarchically structured three-dimensional nickel-iron electrodes for efficient oxygen evolution at high current densities. *Nat. Commun.* **2015**, *6*, 6616.

[23] Bediako, D. K.; Surendranath, Y.; Nocera, D. G. Mechanistic studies of the oxygen evolution reaction mediated by a nickel-borate thin film electrocatalyst. *J. Am. Chem. Soc.* **2013**, *135*, 3662−3674.

[24] Chen, W.; Wang, H. T.; Li, Y. Z.; Liu, Y. Y.; Sun, J.; Lee, S. H.; Lee, J.-S.; Cui, Y. *In situ* electrochemical oxidation tuning of transition metal disulfides to oxides for enhanced water oxidation. *ACS Cent. Sci.* **2015**, *1*, 244−251.

[25] Smith, R. D. L.; Prevot, M. S.; Fagan, R. D.; Zhang, Z. P.; Sedach, P. A.; Siu, M. K. J.; Trudel, S.; Berlinguette, C. P. Photochemical route for accessing amorphous metal oxide materials for water oxidation catalysis. *Science* **2013**, *340*, 60–63.

[26] Zhang, D. D.; Meng, L. J.; Shi, J. Y.; Wang, N.; Liu, S. Z.; Li, C. One-step preparation of optically transparent Ni–Fe oxide film electrocatalyst for oxygen evolution reaction. *Electrochim. Acta* **2015**, *169*, 402–408.

[27] Indra, A.; Menezes, P. W.; Sahraie, N. R.; Bergmann, A.; Das, C.; Tallarida, M.; Schmeißer, D.; Strasser, P.; Driess, M. Unification of catalytic water oxidation and oxygen reduction reactions: Amorphous beat crystalline cobalt iron oxides. *J. Am. Chem. Soc.* **2014**, *136*, 17530−17536.

[28] Kuai, L.; Geng, J.; Chen, C. Y.; Kan, E. J.; Liu, Y. D.; Wang, Q.; Geng, B. Y. A reliable aerosol-spray-assisted approach to produce and optimize amorphous metal oxide catalysts for electrochemical water splitting. *Angew. Chem., Int. Ed.* **2014**, *53*, 7547–7551.

[29] Jin, Z.; Xiao, M. D.; Bao, Z. H.; Wang, P.; Wang, J. F. A general approach to mesoporous metal oxide microspheres loaded with noble metal nanoparticles. *Angew. Chem., Int. Ed.* **2012**, *51*, 6406–6410.

[30] Choi, S. H.; Kang, Y. C. Using simple spray pyrolysis to prepare yolk-shell-structured ZnO-Mn_3O_4 systems with the optimum composition for superior electrochemical properties. *Chem.—Eur. J.* **2014**, *20*, 3014–3018.

[31] Wu, Z.; Huang, X.-L.; Wang, Z.-L.; Xu, J. J.; Wang, H.-G.; Zhang X.-B. Homogeneous β-$Ni(OH)_2$ on graphene with enhanced high-rate cycling for supercapacitors. *Sci. Rep.* **2014**, *4*, 3669.

[32] Huang, J. H.; Chen, J. T.; Yao, T.; He, J. F.; Jiang, S.; Sun, Z. H.; Liu, Q. H.; Cheng, W. R.; Hu, F. C.; Jiang, Y. et al. CoOOH Nanosheets with high mass activity for water oxidation. *Angew. Chem., Int. Ed.* **2015**, *54*, 8722–8727.

[33] U.S. Secretary of Commerce. *NIST XPS Database*. http://srdata.nist.gov/xps/EngElmSrchQuery.aspx (accessed Aug 1, 2015)

[34] Zhang, J. C.; Yang, Y.; Zhang, Z. C.; Xu, X. B.; Wang, X. Rapid synthesis of mesoporous $Ni_xCo_{3-x}(PO_4)_2$ hollow shells showing enhanced electrocatalytic and supercapacitor performance. *J. Mater. Chem. A* **2014**, *2*, 20182–20188.

[35] Li, D. J.; Maiti, U. N.; Lim, J.; Choi, D. S.; Lee, W. J.; Oh, Y.; Lee, G. Y.; Kim, S. O. Molybdenum sulfide/N-doped CNT forest hybrid catalysts for high-performance hydrogen evolution reaction. *Nano Lett.* **2014**, *14*, 1228−1233.